Role of Metabolism in Pathological Aggregation of TDP-43 and its Down-Stream Toxicity

Ismail Gbadamosi, Izabela Lapiarz-Raba, Ali Jawaid*

Laboratory for Translational Research in Neuropsychiatric Disorders, Center of Excellence for Neural Plasticity and Brain Disorders, Nencki Institute of Experimental Biology, Polish Academy of Sciences, Warsaw, Poland. *Correspondence: a.jawaid@nencki.edu.pl

INTRODUCTION

- Amyotrophic lateral sclerosis (ALS) and frontotemporal lobar degeneration (FTLD) are two fatal neurodegenerative disorders with considerable clinical and pathological overlap.
- Both disorders are characterized by the accumulation of pathological aggregates that contain a number of proteins, most notably TAR DNA-binding protein 43 kDa (TDP-43).
- TDP-43 loss-of-function is a potential mechanism in the pathogenesis of ALS and FTLD.
- Conventionally 'risky' metabolic profiles in ALS and FTLD patients have been associated with better clinical outcomes.

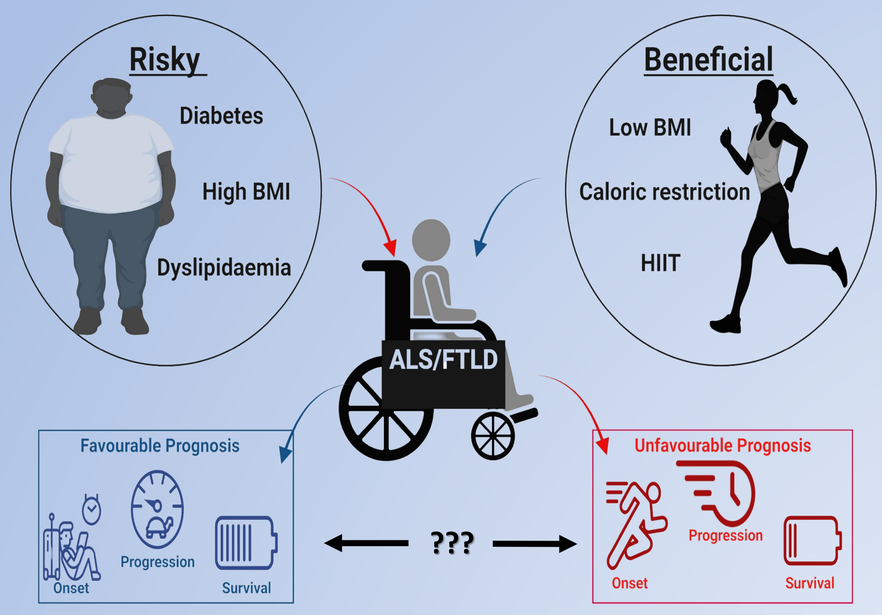

Disease Modifiers in ALS/FTLD

AIM

The initial goal of this study is to understand how TDP43 loss-of-function affects energy metabolism in motor neurons.

METHODS

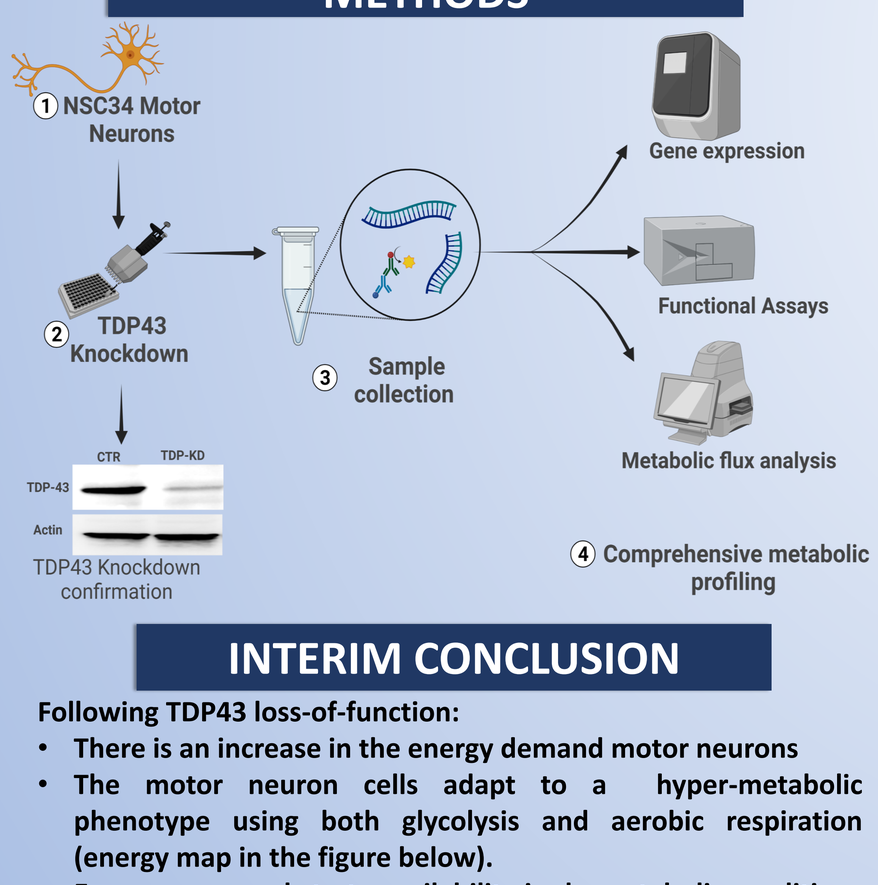

INTERIM CONCLUSION

Following TDP43 loss-of-function:

- There is an increase in the energy demand motor neurons
- The motor neuron cells adapt to a hyper-metabolic phenotype using both glycolysis and aerobic respiration (energy map in the figure below).
- Excess energy substrate availability in dysmetabolic conditions may be beneficial.

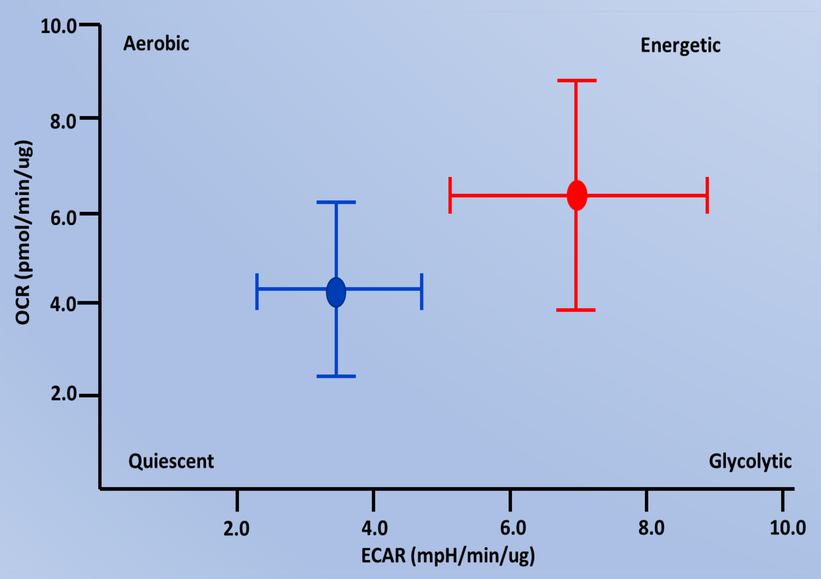

Energy Map in TDP loss-of-function

RESULTS

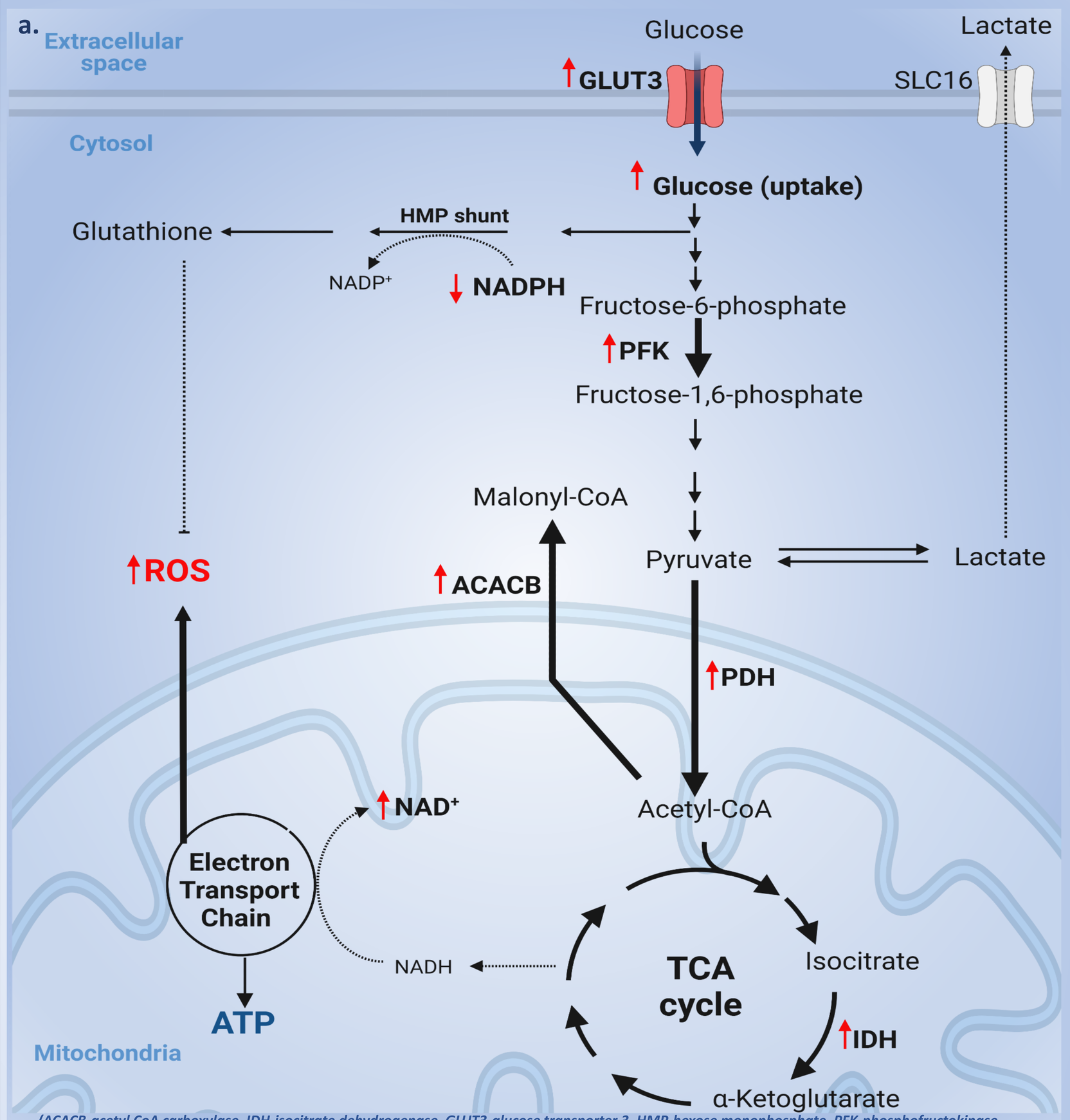

(ACACB-acetyl CoA carboxylase, IDH-isocitrate dehydrogenase, GLUT3-glucose transporter 3, HMP-hexose monophosphate, PFK-phosphofructokinase, PDH-pyruvate dehydrogenase, TCA-tricarboxylic, SLC16-solute carrier 16)

Figure a: The metabolic profile of NSC34 cells following TDP43 loss-of-function shows an increase in glucose uptake and expression of glucose receptors. TDP-43 loss-of-function also increased the expression of rate-limiting enzymes involved in glycolysis, pyruvate metabolism and lipid metabolism.

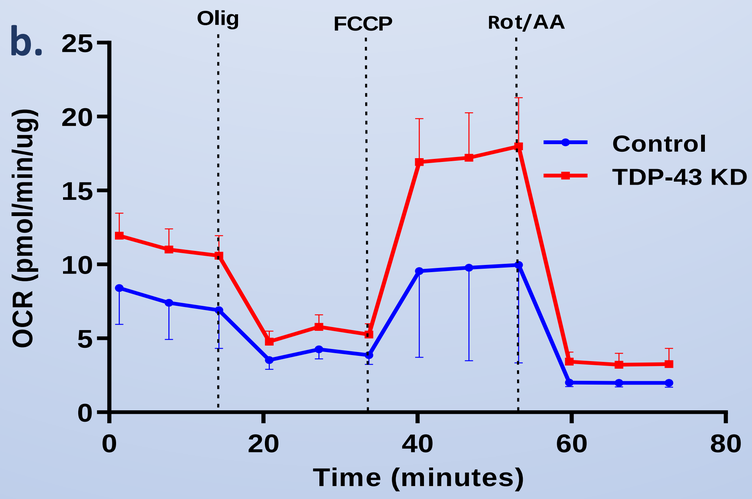

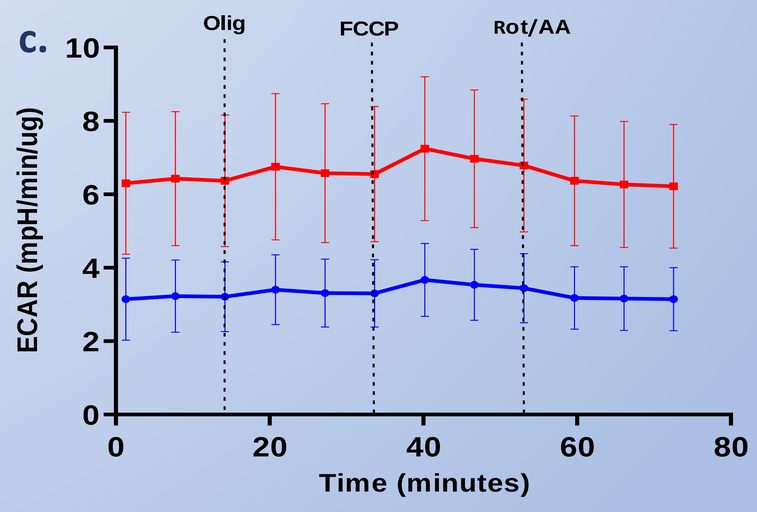

Figures b and c: Metabolic flux analysis reveals an increase in the mitochondrial oxygen consumption rate (b) and extracellular acidification rate (c) TDP43 loss of function.

FUTURE DIRECTIONS

- Identification of the molecular targets underpinning the hypermetabolic status in TDP-43 loss-of-function.
- Manipulation of identified targets for therapeutic potential in 3D neuronal culture model.
- Metabolic phenotyping of motor neurons in TDP-43 aggregation.

nencki institute of experimental biology

This study was supported by the Foundation for Polish Science (Fundacja na rzecz Nauki Polskiej) grant BRAINCITY MAB3.
Illustrations were created with BioRender.com

Fundusze Europejskie Inteligentny Rozwój
Rzeczpospolita Polska
FNP Fundacja na rzecz Nauki Polskiej
Unia Europejska Europejski Fundusz Rozwoju Regionalnego

Characterisation of homozygous FUSΔ14 – ALS mouse model

W Jin[1], B Kalmar[1], N Birsa[1], A Ule[1], M McLaughlin[1], O Wilkins[1], S Bryce-Smith[1], A Brown[1], B Simkin[1], G Price[2], L Greensmith[1], E Fisher[1], T Cunningham[2], P Fratta[1]

[1] Department of Neuromuscular Diseases, UCL Institute of Neurology, Queen Square, London, WC1N 3B, UK
[2] UK MRC Harwell Institute, Harwell Campus, Oxfordshire, OX11 0RD, UK

Introduction

FUSΔ14 **heterozygous** mice are knock-in FUS ALS mouse model with a point-mutation at the intron 13 splice site (13845A>G) and a knocked-in humanized FUS exon 15. They recapitulate many ALS phenotypes at 18 months of age[1].
We have developed **homozygous** FUSΔ14 recently. Compared to the heterozygous model, the homozygous model develops ALS phenotypes more aggressively, showing ALS-like features at 3 months.

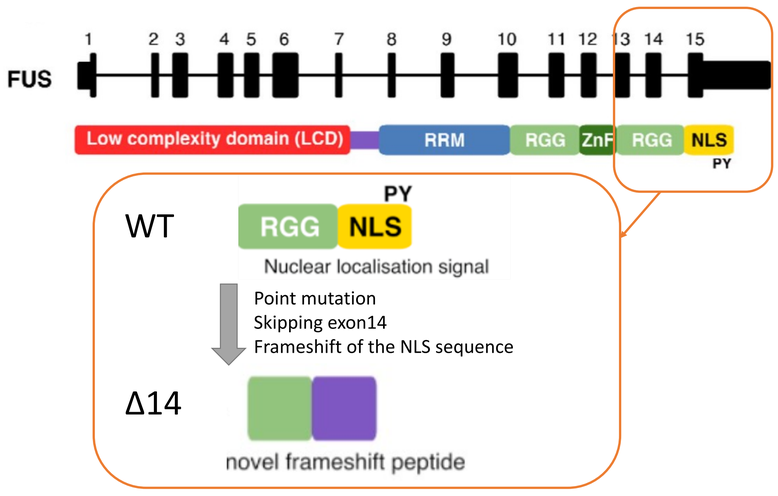

So far, many features have been characterized -

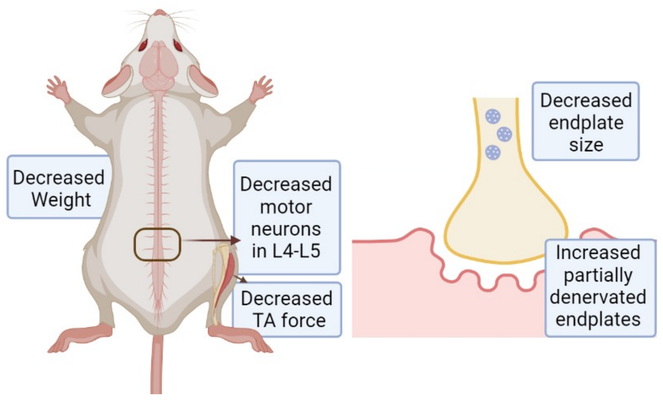

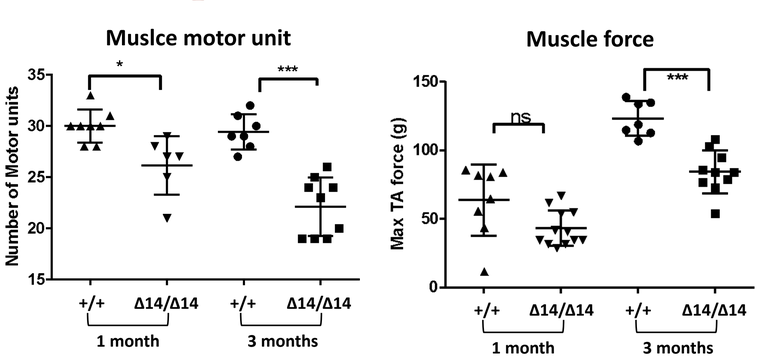

* Left graph: Extensor digitorum longus (EDL) muscle
Right graph: Tibialis anterior (TA) muscle

Our focus of this study is on characterizing this model at the cellular and molecular level.

Method

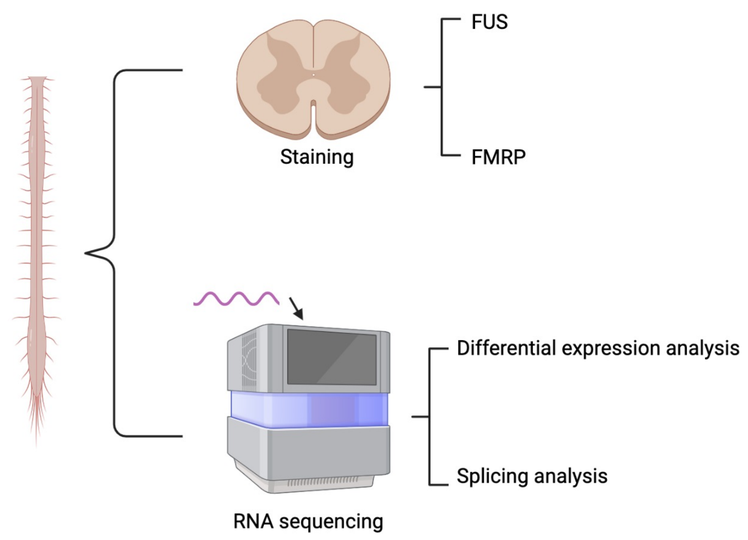

Conclusion

The mislocalisation of FUS in spinal cord causes a series of disruption, including increased expression of FUS via autoregulation, disrupted FMRP equilibrium and a range of transcriptional and translational gene dysregulation.

Result 1: FUS is mislocalised in Δ14 motor neurons

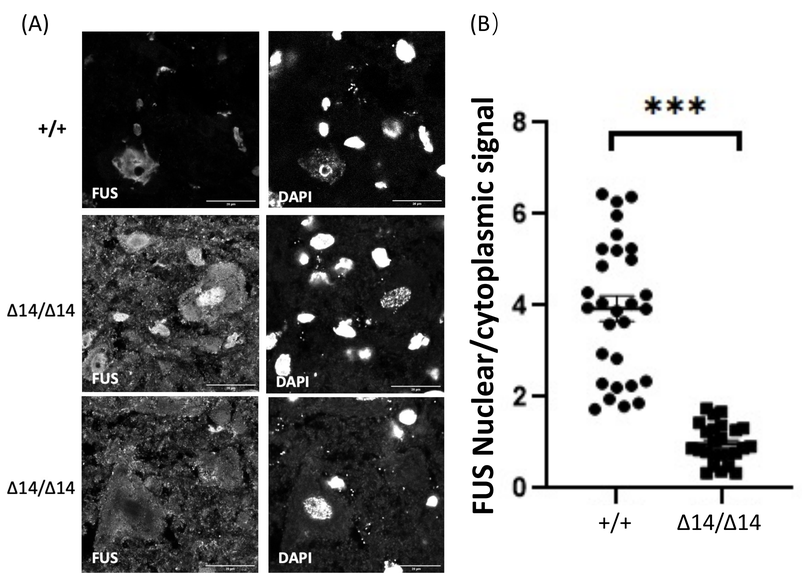

Figure 1: FUS staining of spinal cord lower motor neurons in +/+ and Δ14/ Δ14 spinal cord slices. FUS is mislocalised in Δ14/ Δ14 motor neurons.

(A) Representative gray-scale images of motor neuron staining - FUS and DAPI (nucleus) in split channels. +/+ has FUS restricted in nucleus, while Δ14/ Δ14 shows two phenotypes – either FUS is localized in both cytoplasm and nucleus, or FUS is completely depleted from nucleus.
(B) FUS fluorescence in the nucleus and cytoplasm is analysed as a ratio between the nuclear and cytoplasmic signal (mean ± SEM, +/+ =3.929±0.279, Δ14/ Δ14 =0.9721±0.084, p-value < 0.0001).

Result 3: Increased FMRP puncta in Δ14/Δ14 motor neurons

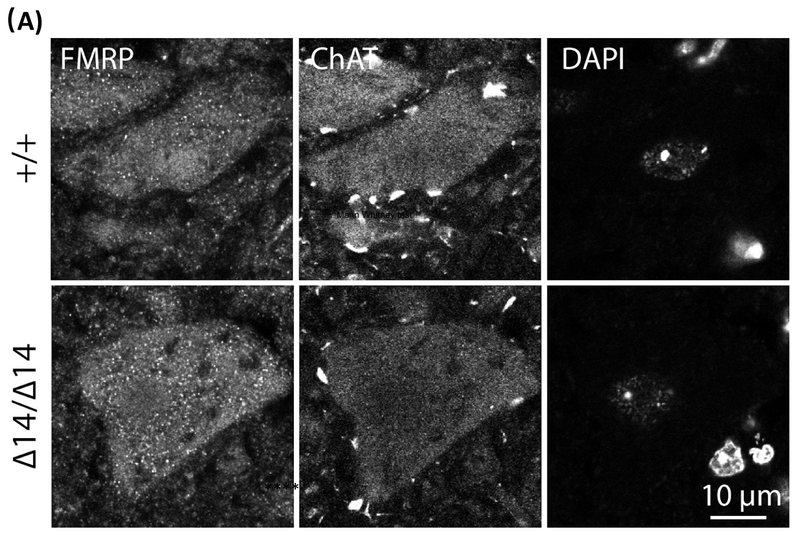

Background:

[1] FMRP is an important protein related to translational repression.
[2] Birsa et al. [2] has found increased FMRP puncta in neuronal axon culture.

Figure 3: FMRP staining of spinal cord lower motor neurons in +/+ and Δ14/ Δ14 spinal cord slices (age: 1 month).

(A) Representative gray-scale images of motor neuron staining – FMRP, ChAT (motor neuron) and DAPI (nucleus) in split channels.
(B) The result of the quantification of the puncta density (puncta count/cell volume). Each colour represents one N (N=6) (Two-tailed Mann-Whitney test, mean ± SEM, +/+ =19.47±3.672, Δ14/ Δ14 =41.41±2.489, p-value < 0.0001).

Result 2: FUS mislocalisation leads to increased levels of its RNA and protein via autoregulation

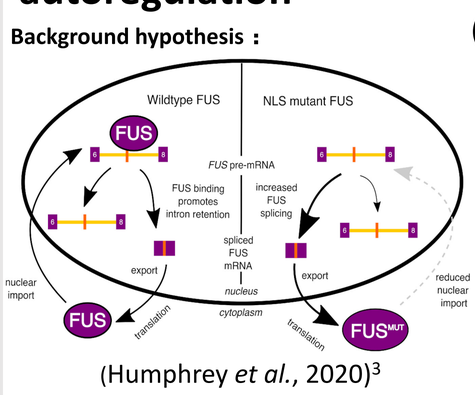

(Humphrey *et al.*, 2020)[3]

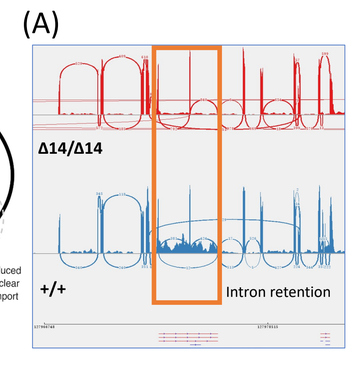

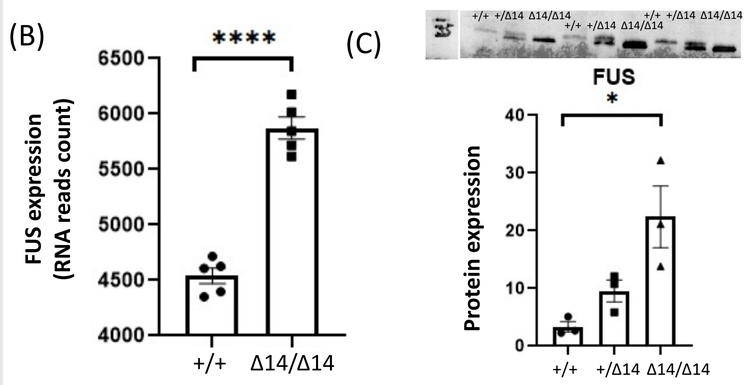

Figure 2: RNA sequencing reveals the increased expression of FUS, probably due to the disruption of the FUS autoregulation mechanism.

(A) The sashimi plot of FUS in +/+ and Δ14/Δ14. Orange box outlines where the intron 6&7 retention is lost in Δ14/ Δ14 .
(B) The comparison of FUS expression between +/+ and Δ14/Δ14. The expression is quantified by the Deseq normalized read counts (mean ± SEM, +/+ =4540±70.49, Δ14/Δ14 =5874±100.7, p-value < 0.0001)
(C) The comparison of FUS protein expression with the western blot, the intensity is normalized to the total protein amount (p-value = 0.004).

Result 4: RNA metabolism disruption is mainly due to FUS nuclear loss-of-function

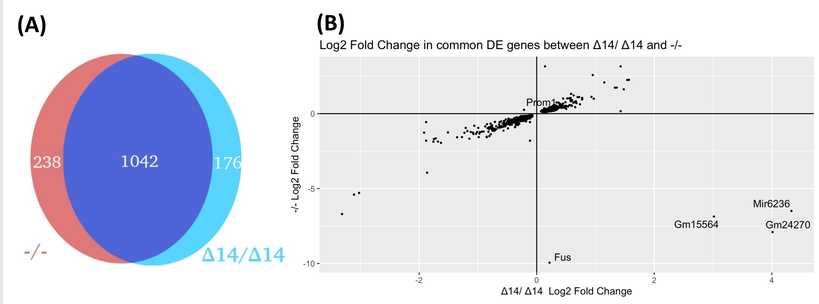

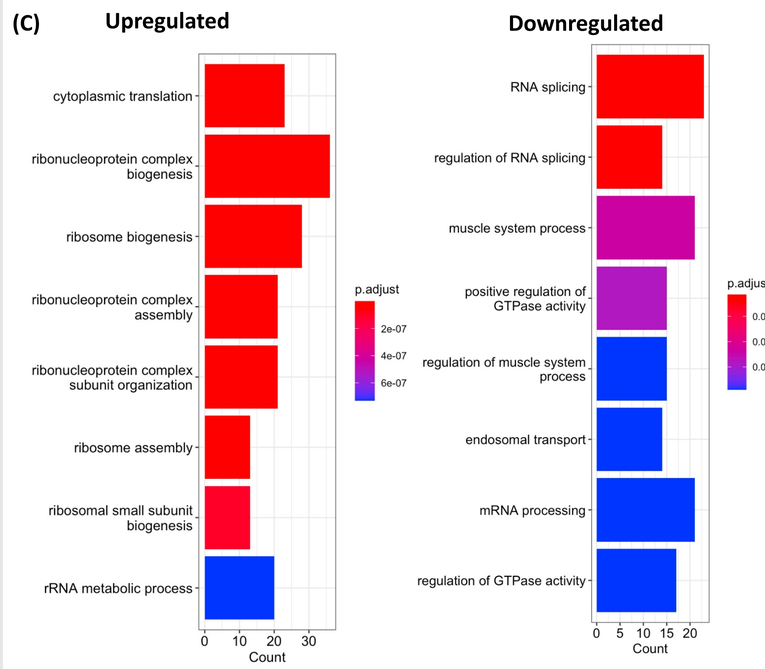

Figure 4: RNA sequencing indicates the transcriptional and translational disruption in Δ14/Δ14 model is due to the loss of function of FUS.
(A) The venn plot of differentially expressed (DE) genes in-/- and Δ14/Δ14. Over 1000 DE genes are the same.
(B) The plot of log2 fold change of Δ14/Δ14 and -/-: although FUS expression changes in different direction, most of the genes are changed in the same direction.
(C) GO analysis result of the common DE genes. Upregulated genes are enriched in translation-related process; while downregulated genes are enriched in RNA splicing, energy-related GTPase activity.

Reference:
1. Devoy, A. *et al.* Humanized mutant FUS drives progressive motor neuron degeneration without aggregation in 'FUSDelta14' knock-in mice. *Brain* **140**, 2797–2805 (2017).
2. Birsa, N. *et al.* FUS-ALS mutants alter FMRP phase separation equilibrium and impair protein translation. *Sci Adv* **7**, eabf8660 (2021).
3. Humphrey, J. *et al.* FUS ALS-causative mutations impair FUS autoregulation and splicing factor networks through intron retention. *Nucleic Acids Res* **48**, 6889–6905 (2020).

STRUCTURAL AND FUNCTIONAL ASPECTS OF MUTATIONS ASSOCIATED TO TYPE B KUFS DISEASE (CLN13)

Tea Sinožić[1,2], Iztok Dolenc[1], and Veronika Stoka[1]

[1]*Department of Biochemistry and Molecular and Structural Biology, J. Stefan Institute, Jamova 39, 1000 Ljubljana, Slovenia*
[2]*Faculty of Medicine, University of Ljubljana, Vrazov trg 2, 1000 Ljubljana, Slovenia*

Abstract Lysosomal cysteine cathepsins belong to the C1 cysteine peptidase family (papain subfamily). They play an important role under physiological conditions, where they are tightly regulated by their endogenous inhibitors. However, if deregulated, they are involved in several pathological processes, including neurodegeneration.
Among eleven human cysteine cathepsins, cathepsin F has unique biochemical and structural properties. However, even two decades after its discovery, many questions still remain unanswered, due to the challenges faced in order to get pure protein in sufficient quantities for its structural and functional characterization.
On the other side, a sequence-based bioinformatics approach was crucial to evaluate the suitability of the wild-type protein from cloning until 3D structure determination by X-ray crystallography. Interestingly, our systematic approach, shows for the first time the bottlenecks that prevented earlier attempts to get this protein using different strategies and/or expression systems. Moreover, on the available 3D structure of the mature form of human cathepsin F, we evaluated the effect of the mutations found in patients, thus associated with an adult-onset neuronal ceroid lipofuscinosis, namely Type B Kufs disease (CLN13). These results, clearly showed a destabilizing effect of all evaluated mutants, thus providing the structural basis for the detrimental effect observed in functional studies.

Human cathepsin F protein production using MilliporeSigma's next generation cell free protein expression system (Wheat Germ)

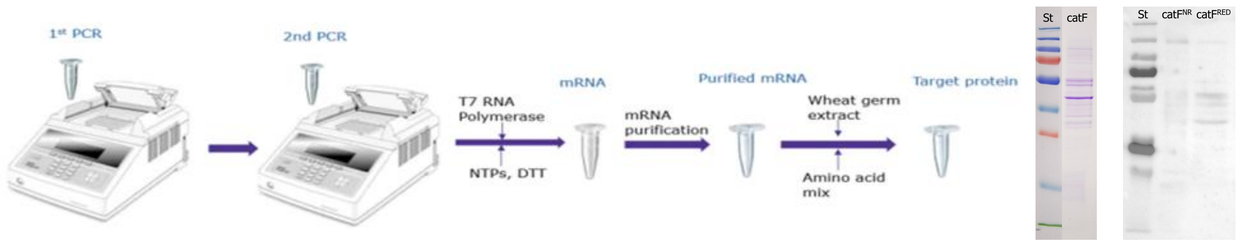

Schematic representation of human cathepsin F (wtCatF) and CLN13 mutations

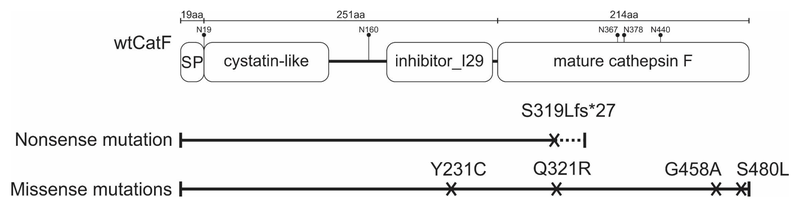

Evolutionary conservation of human cathepsin F [1] predicted using ConSurf [2]

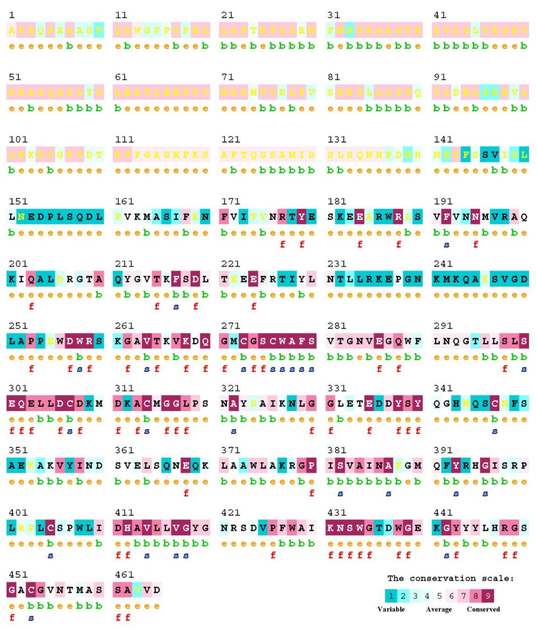

Proposed 3D model of human cathepsin F

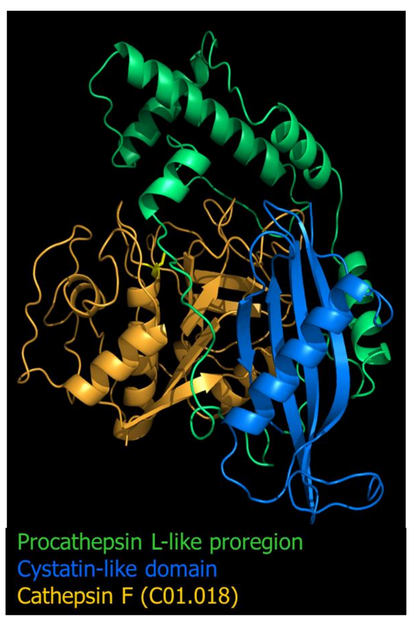

Localization of CLN13 mutations on the 2D plot (A) and cartoon representation (B) of the mature form of human cathepsin F (1M6D:A) [5]

A

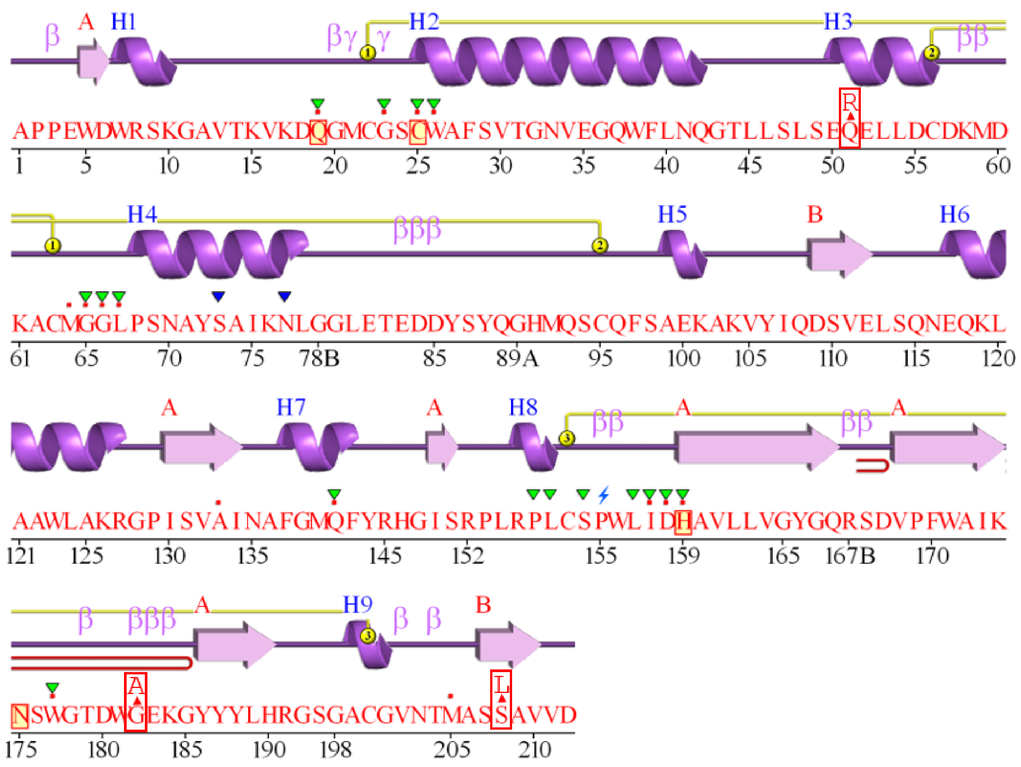

B

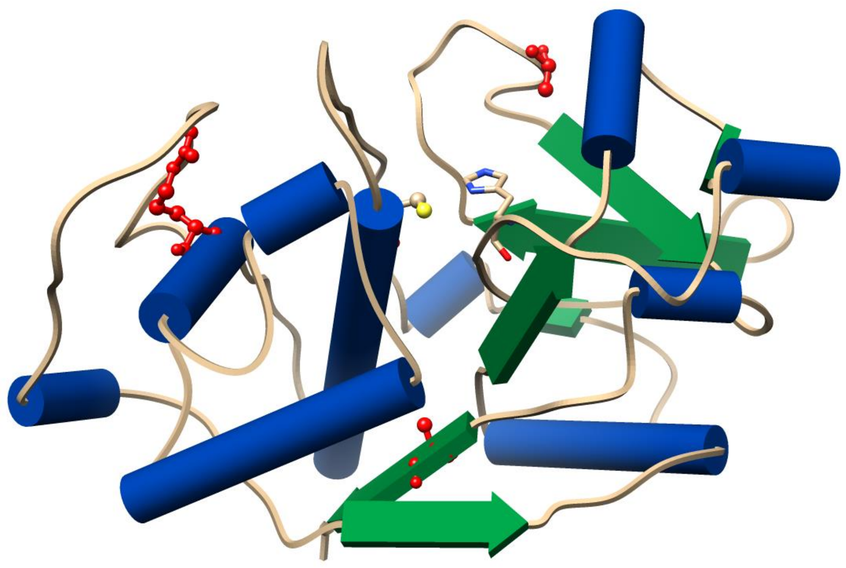

Type B Kufs disease pedigrees [4]

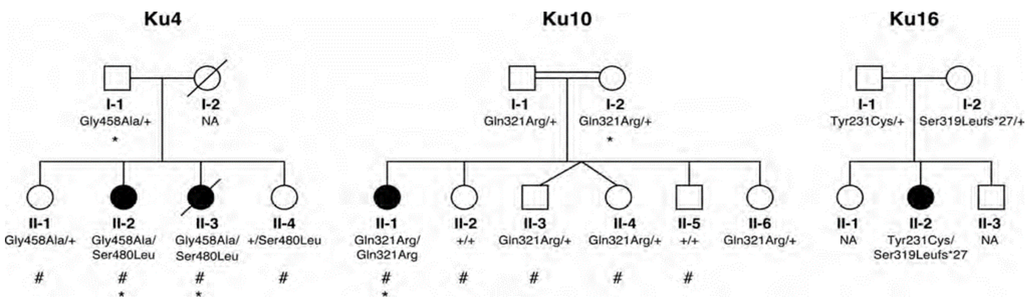

Family Ku4: Brain pathology of the proband (II-3) [4]

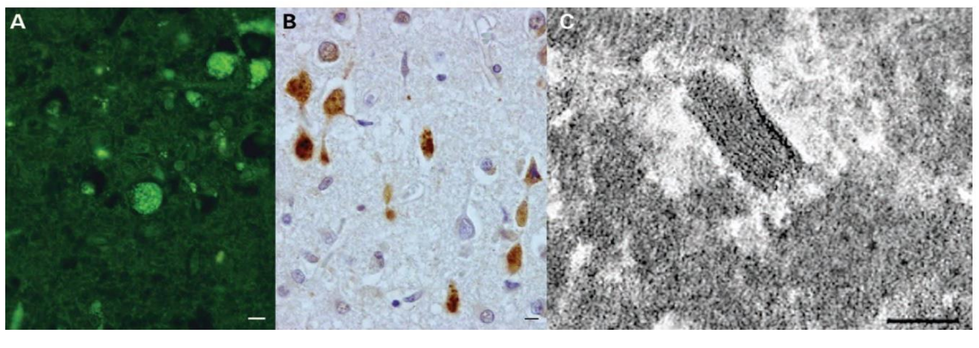

Table 1. Neuronal ceroid lipofuscinosis-related proteins with their molecular characteristics, postulated function, interactions and lipid phenotype [3]

NCL-related protein name	Other names/ synonyms	Protein size and structural features	Posttranslational modification	Protein localization	Function	Interactions	Abnormal lipid composition[a]
CLN1	Palmitoyl protein thioesterase 1 (PPT1)	306 aa, soluble protein	*N*-gly M6P	Lysosomal matrix, extralysosomal vesicules, extracellular	Palmitoylthioesterase	S-acetylated proteins (GAP43, rhodopsin, saposin D)	Phospholipids, ceramide, cholesterol
CLN2	Tripeptidyl peptidase 1 (TPP1)	563 aa, soluble protein	*N*-gly M6P	Lysosomal matrix	Serine protease	CLN3, CLN5	n.d.
CLN3	–	438 aa, 6 TM protein	*N*-gly farnesylated phosphorylated	Late endosomal/lysosomal membrane, presynaptic vesicles	Unknown; modulation of vesicular trafficking and fusion, pH regulation	Hook1, Rab7, fodrin, kinesin-2, CLN5, Na^+, K^+ATPase	BMP, Phospholipids, galactosyl-ceramide
CLN4	Cysteine-string protein alpha (CSPα), DNAJC5	198 aa, soluble protein	Palmitoylated	Cytosolic, associated to vesicular membranes	Hsc70 co-chaperone, involved in exocytosis and endocytosis	CSPα, Hsp70, Hsp40, Hsp90, HIP, HOP, SGT, SNAP-25, dynamin-1, syntaxin, Gαs, Rab3b, synaptotagmin 9, myosin IIB, calsenilin, DHHC17	n.d.
CLN5	–	407 aa, soluble protein	*N*-gly M6P	Lysosomal matrix	Unknown; modulation of vesicular trafficking predicted	PPT1/CLN1, TPP1/CLN2, CLN3, CLN6, CLN8	Sphingolipids
CLN6	–	311 aa, 7 TM protein	None	ER-membrane	Unknown	CLN5, CLN6 CRMP-2	Phospho- and glycosphingo-lipids, cholesterol
CLN7	–	518 aa, 12 TM protein	*N*-gly proteolytic cleaved	Lysosomal membrane	Unknown; transmembrane transporter function predicted	AP-1, cathepsin L	n.d.
CLN8	–	286 aa, 5 TM protein	None	ER/ERGIC-membrane	Unknown; regulation in lipid metabolism predicted	CLN5, CLN8, VAPA, GATE16, syntaxin 8	Ceramides, phospholipids, sphingolipids, sulfatides
CLN9 (postulated)	Unknown	–	–	–	Unknown, role in ceramide synthesis postulated	–	Ceramide, sphingomyelin, sphingolipids, globosides
CLN10	Cathepsin D (CTSD)	462 aa, soluble protein	*N*-gly M6P	Lysosomal matrix, extracellular	Aspartyl endopeptidase	APP, CST3, CTSB, proSAP, and several others	BMP, cholesterol, phospho- and sphingolipids
CLN11	Progranulin, proepithelin, acrogranin	593 aa, soluble protein	None	Extracellular	Unknown, roles in inflammation, embryogenesis, cell motility and tumorigenesis postulated	MMPs, ADAMs, TGFα receptors, sortilin, ADAMTS-7/ADAMTS-12/perlecan/HDL/ COMP	n.d.
CLN12	ATPase 13A2, KRPPD, PARK9, HSA9947, RP-37C10.4	1180 aa, 10 TM protein	None	Lysosomal membrane	Unknown; regulation of ion homeostasis postulated	Interaction to 43 proteins involved in vesicular trafficking and synuclein misfolding postulated	n.d.
CLN13	Cathepsin F (CTSF)	484 aa, soluble protein	*N*-gly M6P	Lysosomal matrix	Cysteine protease	CD47 antigen	n.d.
CLN14	Potassium channel tetramerization domain-containing protein 7 (KCTD7)	289 aa, soluble protein	Phosphorylated	Cytosolic, partially associated to membranes	Unknown; modulation of ion channel activity predicted	Cullin-3, KCTD7	n.d.

aa, amino acids, TM, transmembrane domains, M6P, mannose 6-phosphate, *N*-gly, *N*-glycosylation, BMP, bis(monoacylglycero)phosphate, n.d., not described.
[a] In addition to the common lipopigment storage.

Table 2. Effect of CLN13 mutations on the stability of human cathepsin F (1M6D:A) [5] calculated using CUPSAT [6]

Mutation site		Structural Features			Experimental Method - Thermal		
Protein sequence Q9UBX1	Protein structure 1m6d:A	SS element	Solvent accessibility	Torsion angles (φ, ψ)	Overall Stability	Torsion	Predicted ΔΔG (kcal/mol)
Gln321Arg	Gln51Arg	Helix	0.0%	-60.0°, -38.9°	Destabilising	Favourable	-4.74
Gly458Ala	Gly182Ala	Other (turns, coils, etc.)	17.79%	56.5°, -145.7°	Destabilising	Unfavourable	0.64
Ser480Leu	Ser208Leu	Sheet	0.0%	-157.4°, 148.1°	Destabilising	Unfavourable	-4.02

References

[1] Nägler DK, Sulea T, Ménard R. Full-length cDNA of human cathepsin F predicts the presence of a cystatin domain at the N-terminus of the cysteine protease zymogen. *Biochem Biophys Res Commun*. 1999;257(2):313-8. doi: 10.1006/bbrc.1999.0461
[2] Ashkenazy H, Abadi S, Martz E, Chay O, Mayrose I, Pupko T, Ben-Tal N. ConSurf 2016: an improved methodology to estimate and visualize evolutionary conservation in macromolecules. *Nucleic Acids Res*. 2016;44(W1):W344-W350. doi:10.1093/nar/gkw408
[3] Kollmann K, Uusi-Rauva K, Scifo E, Tyynelä J, Jalanko A, Braulke T. Cell biology and function of neuronal ceroid lipofuscinosis-related proteins. *Biochim Biophys Acta*. 2013;1832(11):1866-81. doi: 10.1016/j.bbadis.2013.01.019
[4] Smith KR, Dahl HH, Canafoglia L, Andermann E, Damiano J, Morbin M, Bruni AC, Giaccone G, Cossette P, Saftig P, Grötzinger J, Schwake M, Andermann F, Staropoli JF, Sims KB, Mole SE, Franceschetti S, Alexander NA, Cooper JD, Chapman HA, Carpenter S, Berkovic SF, Bahlo M. Cathepsin F mutations cause Type B Kufs disease, an adult-onset neuronal ceroid lipofuscinosis. *Hum Mol Genet*. 2013;22(7):1417-23. doi: 10.1093/hmg/dds558
[5] Somoza JR, Palmer JT, Ho JD. The crystal structure of human cathepsin F and its implications for the development of novel immunomodulators. *J Mol Biol*. 2002;322(3):559-68. doi: 10.1016/s0022-2836(02)00780-5
[6] Parthiban V, Gromiha MM, Schomburg D. CUPSAT: prediction of protein stability upon point mutations. *Nucleic Acids Res*. 2006;34(Web Server issue):W239-W242. doi:10.1093/nar/gkl190

A multi-omics approach to study monozygotic twins discordant for Amyotrophic Lateral Sclerosis

M. Tosi[1], M. Zuccalà[1], F. Favero[1], L. Corrado[1], R. Croce[1], C. Basagni[1], N. Barizzone[1], L. Follia [1], A.S. Costa [1], F. De Marchi[2], E. Chinni[3], L. Mazzini[2], D. Corà[1], M. Leone[4], S. D'Alfonso[1]

1 University of Eastern Piedmont UPO, Novara, Italy
2 ALS Center AOU Maggiore della Carità, Novara, Italy
3 Thrombosis and Haemostasis Unit, Fondazione I.R.C.C.S. "Casa Sollievo della Sofferenza", S. Giovanni Rotondo, Foggia, Italy
4 SC Neurologia, Dipartimento di Scienze Mediche, IRCCS Casa Sollievo della Sofferenza, San Giovanni Rotondo, Foggia, Italy

Introduction and aim of the study

Amyotrophic lateral sclerosis (ALS) is a fatal neurodegenerative disease, characterised by progressive death of upper and lower motor neurons. 90% of patients have no prior family history (sporadic ALS), while 10% of ALS patients have at least one other affected family member (familial ALS). This disease is phenotypically heterogeneous and its etiology is still poorly understood, as both genetic susceptibility and environmental exposure contribute to the pathogenesis.

To investigate genetic and epigenetic factors underlying ALS, we studied a monozygotic twin pair discordant for ALS. We applied a multi-omics approach, combining whole exome sequencing with genome-wide methylome- and transcriptome data from whole blood and PBMCs.

Materials and Methods

Transcriptome Analysis

- 8 samples: biological duplicate and, for the second blood sample, a technical triplicate
- 100 ng of RNA from PBMCs; library kit: Illumina TruSeq Stranded mRNA. mRNA sequencing was performed using NextSeq 500/550 High Output Kit v2.5 (150 Cycles - 2 X 75 read length, paired-end), obtaining a mean of 50 million reads per sample
- Quality controls were assured using FastQC. Data were analyzed with RSEM and STAR for the alignment of reads to the reference genome (GRCh38/hg38). We evaluated differentially expressed genes (DEGs) by DESeq2 with p.value adj < 0.1 and |log2FC|> 1. Lastly, pathway analysis has been conducted with different bioinformatic tools as G-Profiler, ToppGene, GSEA and IPA

Methylation Analysis

- 8 samples: a biological duplicate and, for each blood sample, a technical duplicate
- 500 ng of DNA from whole blood converted by using bisulphite conversion technique. We used the Infinium Methylation EPIC Array scanned on the NextSeq 550.
- Quality controls were performed on Illumina GenomeStudio software. Results were analyzed using both GenomeStudio and the Chip Analysis Methylation Pipeline (ChAMP) Bioconductor package that allow the identification of differentially methylated probes (P.value adj ≤ 0.1; Δβ ≥ 0.25; Δβ ≤ - 0.25)

Whole Exome Sequencing

- 2 samples: one blood sample per subject
- 50 ng of DNA according to Agilent Sure Select QXT Kit. WES has been processed using NextSeq 500/550 High Output Kit v2, producing 2x150 bp read lengths and 30X coverage across samples
- Fastq files were aligned on GRCh37 genome and BWA software produced the bam files. For each patient, a list of variations in a VCF format file was produced by GATK software and annotation of VCF files was performed by wANNOVAR software. CNV analysis has been performed by ExomeDepth tool. We tested ALS vs healthy twin and healthy vs ALS twin; then variants were classified as benign, pathogenic or of uncertain significance by ClassifyCNV Scores

Results

Transcriptome Analysis

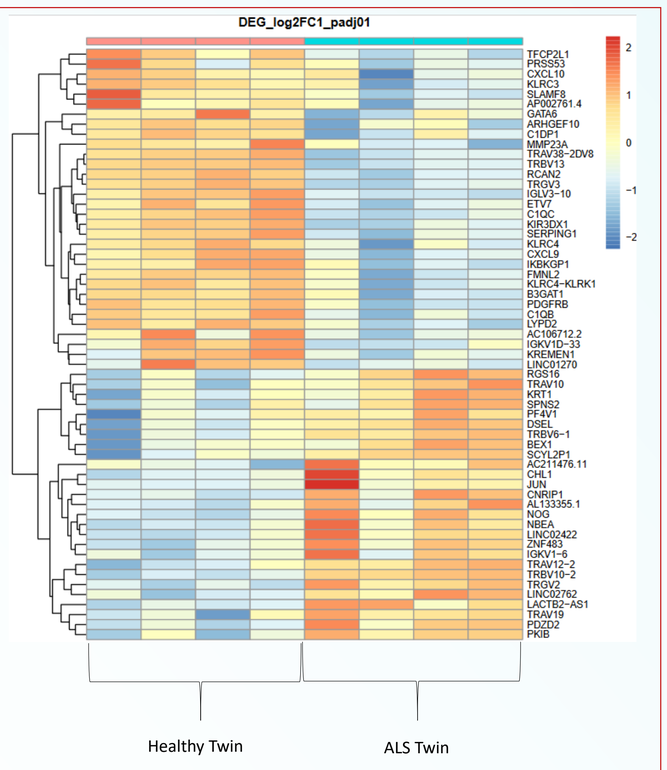

Figure 1: The heatmap shows the identified 59 DEGs for the healthy twin (left) and the ALS twin (right). Upregulated genes are represented in the red scale, while downregulated genes in the blue scale. On the right there are genes name, on the left genes are clustered by similar expression values

Methylation Analysis

pvalue adj ≤ 0.1	P.Value Adj	CHR:POS	Gene	Cgi
cg18454685	0,004060966	17:48639239	CACNA1G	Body-island
cg27533288	0,054051711	10:118896776	VAX1	Body-island

Δβ ≤ - 0.25	Δβ	P.Value Adj	CHR:POS	Gene	Cgi
cg18686665	-0,2899808	0,692505608	2:629121		IGR-island
cg01032200	-0,3178169	0,711717766	1:155290641	RUSC1-AS1	Body-island

Δβ ≥ 0.25	Δβ	P.Value Adj	CHR:POS	Gene	Cgi
cg18565204	0,4725682	0,598885039	16:70298926	AARS	Body-opensea
cg18987683	0,2675134	0,915051596	3:160283058	KPNA4	1stExon-island

Table 1: Differentially Methylated Probes identified, based on p.value adj ≤ 0.1 or Δβ ≤ - 0.25 and Δβ ≥ 0.25

Figure 2: Example of 2 out of 6 validated DEGs by ddPCR. SERPING is confirmed to be downregulated in the ALS twin, while PF4V1 is upregulated. HPRT1 is the housekeeping gene

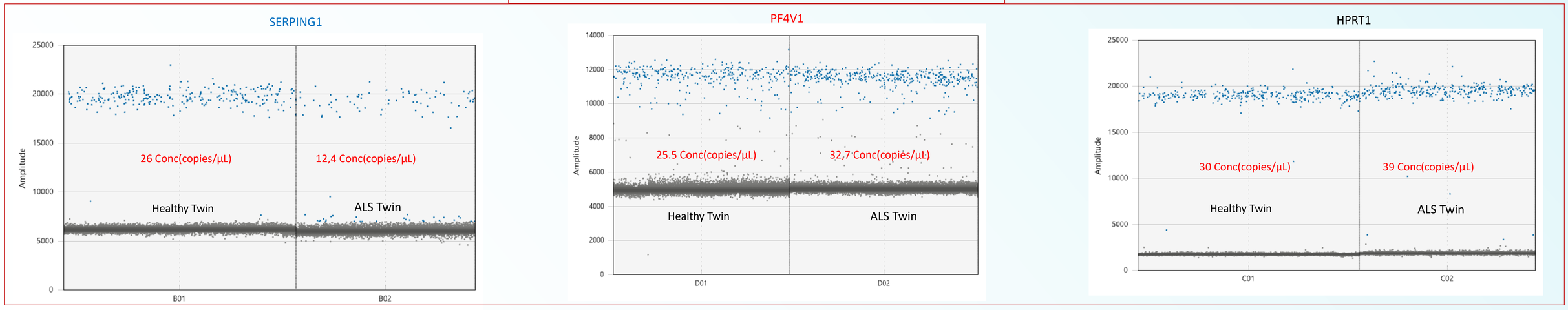

Whole Exome Sequencing

SNV	Healthy Twin vs ALS Twin	ALS Twin vs Healthy Twin
Different Variants	109	162
Pass Variants	10	25
Position	8 exonic 2 intronic	15 exonic 10 intronic
Exonic Function	3 synonymous 4 nonsynonymous 1 nonframeshift deletion	5 synonymous 8 nonsynonymous 1 nonframeshift deletion 1 nonframeshift insertion

Table 2: summary of SNVs identified in the ALS twin filtered for gnomAD_EXOME_ALL ≤ 0,00005 OR frequency 0

CNV	Healthy Twin vs ALS Twin	ALS Twin vs Healthy Twin
Deletions	2 of uncertain significance	3 of uncertain significance
Duplication	2 of uncertain significance	1 of uncertain significance

Table 3: summary of specific CNVs different for 60% and identified in the ALS twin

Conclusion

We studied a discordant twin pair for ALS considering three different omics, independently and in combination, to identify disease-relevant changes. Twins tested negative for mutations in main ALS-genes. From RNA-seq we identified 59 DEGs and validated 6 DEGs by ddPCR; functional analyses with distinct bioinformatic tools underlined a possible role of the immune system in the disease, as partially described in literature. We also identified 2 differentially methylated probes in *CACNA1G*, expressed mostly in brain, and *VAX1* genes and, filtering by Δβ values, we found 2 probes with Δβ ≤ - 0.25 in an intergenic region and in *RUSC1-AS1* gene and 2 probes with Δβ ≥ 0.25 in *AARS* and *KPNA4* genes. For exome analyses, 3 deletions and 1 duplication of uncertain significance were identified only in the ALS twin, while filtering for frequency and QC we were able to identify 25 variants (15 exonic, 10 intronic). Further understanding of these immunological results and the validation of methylation results by methylation-specific droplet digital PCR (ddMSP) combined with methylation-dependent restriction enzymes are ongoing to elucidate possible somatic genetic factors that could underlie susceptibility to sporadic ALS.

ICGEB – ALS Society of Canada Symposium on Inflammation and Proteinopathy in ALS/FTD Spectrum Disorder. Rijeka, Croatia; June, 30 – July, 3 2022

Authors declare no conflict of interest

Computational Study of the Monoamine Oxidase B Mechanism-Based Irreversible Inhibitors

Lucija Vrban[1], Željko Svedružić[1], Robert Vianello[2]

[1]Biomolecular Structure and Function Group, Department of Biotechnology, Rijeka, Croatia
[2]Laboratory for the Computational Design and Synthesis of Functional Materials, Ruđer Bošković Institute, Zagreb, Croatia
lucija.vrban@uniri.hr

INTRODUCTION

- MAO B metabolizes monoamine neurotransmitters like dopamine in its 'aromatic cage' during oxidative deamination
- MAO B amplifies symptoms of Parkinson's disease and other neurodegenerative disorders [1]
- Selegiline and rasagiline follow hydride abstraction mechanism [3]
- An innovative approach: aromatic scaffolds [2] + propargylamine core

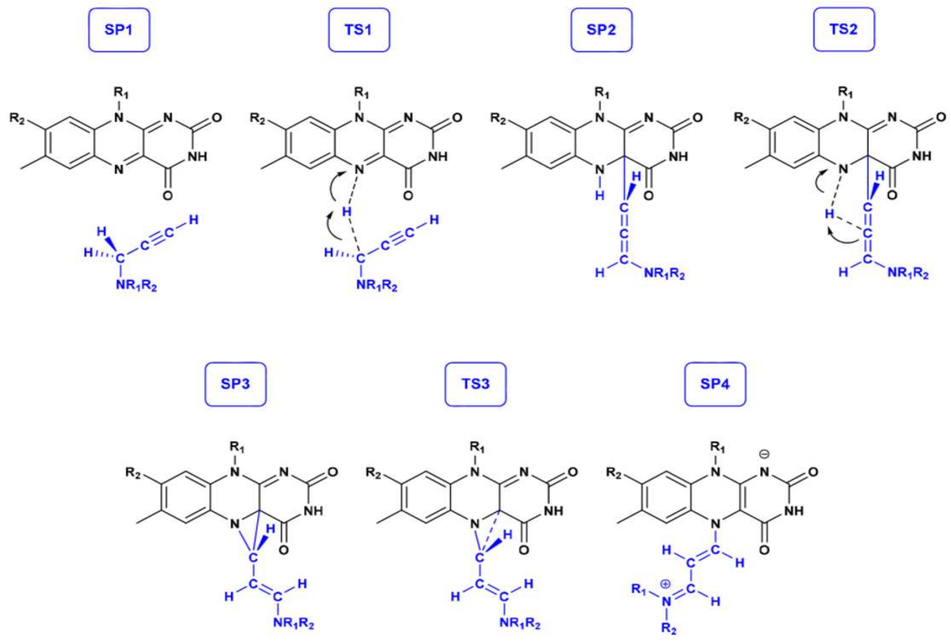

Figure 1 Chemical structures corresponding to stationary points (SP) and transition states (TS) during the irreversible MAO inhibition reaction [1].

CHALLENGES AND MAIN GOAL

- Neurodegenerative diseases are 5th cause of death worldwide and rising
- Commerical drugs are administrated with dietary restrictions and lose selectivity in high doses [1]

Mechanism-based inhibitors with better thermodynamic and kinetic reaction profiles

MATERIALS AND METHODS

- Drug design in PyMOL
- Batch molecular docking using Autodock Vina *via* UCSF Chimera interface
- All-atom molecular dynamics simulations in duration of 300 ns using GROMACS
- Quantum-mechanical cluster approach done in Gaussian

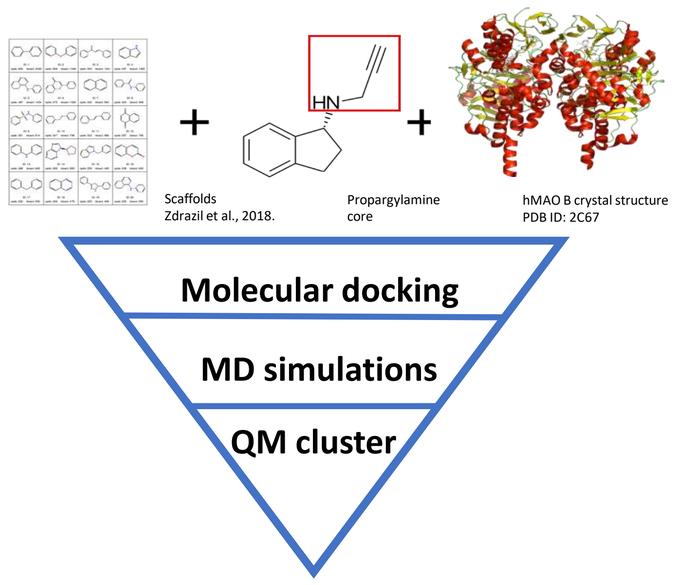

Figure 2 Graphical scheme of the workflow.

RESULTS

Table 1 Computed Gibbs binding free energy of the newly designed molecules and control molecules; selegiline and rasagiline. *Energy obtained from MD simulations via g_mmpbsa package.*

Ligand	ΔG_{bind} (kcal/mol)
42H	-22.00
42Me	-21.54
258H	-22.71
SEL	**-20.04**
RAS	**-18.07**

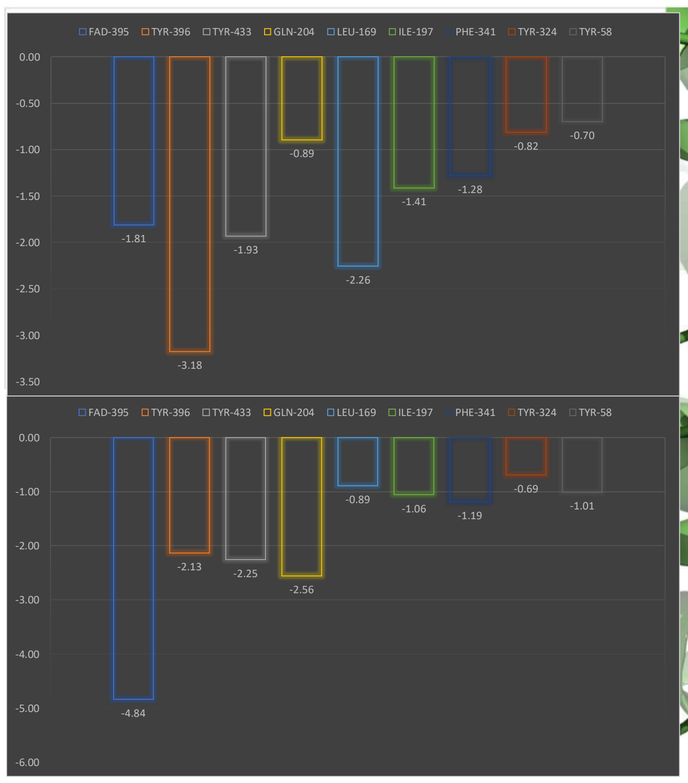

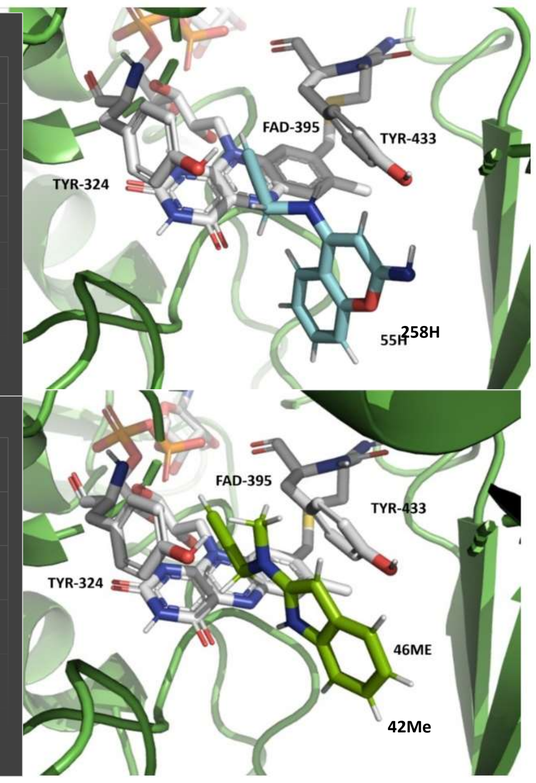

Figure 3 Per residue energy decomposition and the 'aromatic cage' of MAO B active site with docked molecules; 42H, 42Me and 258H. *Computed contribution to the Gibbs binding free energy (obtained from MD simulations using MM-PBSA approach and free energy decomposition per residue) in kcalmol^{-1}. Per residue energy decomposition follows analysis the same trend in control molecules as in newly designed candidates.*

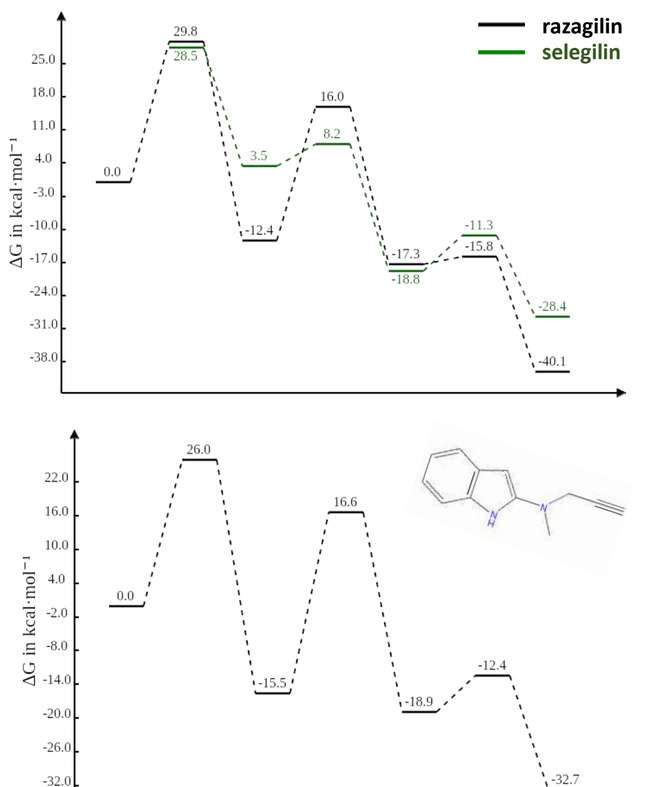

Figure 4 Free-energy profiles for the irreversible MAO B inhibition with 42Me. *Acronyms SP and TS indicate stationary points and transition states, respectively. Chemical structures are depicted in Figure 1.*

RESOURCES

CONCLUSIONS

- Hit compound: 42Me
- Obtained thermodynamic and kinetic reaction profiles are more favourable compared to commercial drugs
- 42Me follows hydride abstraction mechanism

BIBLIOGRAPHY

[1] T. Tandarić, A. Prah, J. Stare, J. Mavri, R. Vianello, *Int. J. Mol. Sci.* 21 (2020) 6151.
[2] B. Zdrazil, R. Guha, *J. Med. Chem.* 61 (2018) 4688–4703.
[3] T. Tandarić, R. Vianello, *ACS Chem. Neurosci.* 10 (2019) 3532–3542.